# 6

# Janus WSSe and WSeTe buffer layer for WS2 and WSe2 absorber materials based solar cells

## 6.1 Introduction

The TMDs based hexagonal phase bulk $WS_2$ and $WSe_2$ materials exhibit semiconducting nature with indirect bandgap. In addition, reducing the dimension from bulk 3D system to 2D monolayer switches to direct bandgap semiconductor (G. Bin Liu, Xiao, Yao, Xu, & Yao, 2015). The reported results suggest that $WS_2$ is the n-type semiconductor and deposited on the p-type silicon substrate for solar cell devices (Wen et al., 2017). Tungsten based TMDs materials reported the very high absorption towards the incident solar radiation, which ensures the potential absorber materials for solar cell applications (L. Ma et al., 2017; Roy & Bermel, 2018). TMDs based materials are used in the photovoltaic device in two different ways: (a) efficiency booster together with other semiconductor materials like Si and GaAs and (b) efficient absorber (Akama et al., 2017). Continuous efforts are made on fabricating TMDs based solar cell devices (Furchi et al., 2017; Singh, Kim, Yeom, & Nalwa, 2017; Thilagam, 2017; Yu & Sivula, 2016). The efficiency of the solar cell depends on the bandgap and absorption coefficient over the solar spectrum. TMDs based materials have very high absorption and absorb 5-10% solar light in the bilayer (Bernardi, Palummo, & Grossman, 2013). Ultrathin WSSe and WSeTe monolayers have direct bandgap semiconductor nature, which can be used as a buffer layer for solar cell applications (Guan, Ni, & Hu, 2018).

The optoelectronic properties of Janus WSSe and WSeTe monolayers are found to be suitable as a buffer layer and bulk $WS_2$ and $WSe_2$ as the absorber layers for solar cell applications. The other electronic parameters required for simulating the solar cell performance are derived from optoelectronic properties. Here, we have used the AZO, i.e., Al-doped ZnO, as the front contact and $W(S/Se)_2$ as the absorber materials in a solar cell. The solar cell performance is simulated using a SCAPS-1D based on the properties computed using the DFT. The effect of absorber layer thickness, carrier concentration, and defect density on the PV performance of the solar cell is analysed. The effect of thickness and carrier concentration of buffer layer on PV performance is also analysed. The interface defect density at the interfaces of heterojunction devices has a significant effect on the solar cell performance. We observed the impact of various parameters on PV performance, and the optimized performance of the solar cell is reported in this chapter.

## 6.2 Methodology

The full potential linear augmented plane wave method as implemented in the WIEN2k package is used to calculate the ground state properties of bulk materials ($WS_2$ and $WSe_2$) and ultrathin Janus WSSe and WSeTe monolayers (Blaha & Madsen, 2016). The exchange-correlation energy is predicted using the GGA-PBE exchange-correlations (Perdew, Burke, & Ernzerhof, 1997). As GGA-PBE approach is not suitable for predicting the optoelectronic properties, mBJ exchange-correlation is used. The mBJ is considered as one of the most accurate methods to

predict the optoelectronic properties (Tran & Blaha, 2009). The muffin tin radii of the considered atoms are chosen sufficiently large to avoid their overlapping. The plane wave cutoff parameters are $R_{mt}*K_{max}$ = 7 and $G_{max}$ = 12 throughout the calculation. The core and valence electrons are separated by the -6.0 Ry. The structural parameters, including the atomic position and lattice parameters, are optimized by reducing the total energy and force cut off at $1x10^{-4}$Ry and $1x10^{-3}$Ry/au for the unit cell. The structural optimization is carried out using 500 K-points, and further the optoelectronic properties are calculated using 5000 K-points. The reflection from the top surface of the buffer layer is considered zero, and the reflection from the bottom surface is assumed 100%. The PV performance of the solar cell is simulated against AM 1.5G illumination and solving the one-dimensional basic semiconductor equations.

## 6.3 Results and Discussion

The hexagonal structure of bulk $WS_2$ and $WSe_2$ have trigonal prismatic symmetry, in which the tungsten element is placed between the S/Se atoms. The in-plane atoms are connected through the covalent bonding, and out-of-plane layers are interacted through vdW force, shown in Figure 6.1. The optimized structural parameters are listed in table 6.1 and are in agreement with the reported results (Coehoorn et al., 1987; Schutte, De Boer, & Jellinek, 1987). Similarly, ultra-thin Janus WXY structures are built by exchanging the top layer of Se atoms of $WSe_2$ monolayer by S/Te atoms. The optimized parameters of ultra-thin WSSe and WSeTe structures are optimized, and lattice constants are 3.25 and 3.44 Å, respectively, which are approximately equal to the computationally reported results (Er et al., 2018; S.-D. Guo, 2018). Ultra-thin Janus monolayers break the mirror symmetry due to the presence of two different chalcogen elements. The structural parameters of WSSe and WSeTe are listed in table1.

**Table6.1** Structural parameters of bulk absorber material and Ultra-thin Janus structures.

| System | Lattice parameters (Å) | Bond length (Å) | | Angle (°) | | |
|---|---|---|---|---|---|---|
| | | W-X | W-Y | ∠XWX | ∠ XWY | ∠YWY |
| $WS_2$ | 3.18, 12.50 | 2.452 | | 83.023 | | |
| $WSe_2$ | 3.28, 12.96 | 2.526 | | 82.800 | | |
| WSSe | 3.25 | 2.427 | 2.546 | 84.061 | 81.894 | 79.318 |
| WSeTe | 3.44 | 2.565 | 2.732 | 84.188 | 82.672 | 78.00 |

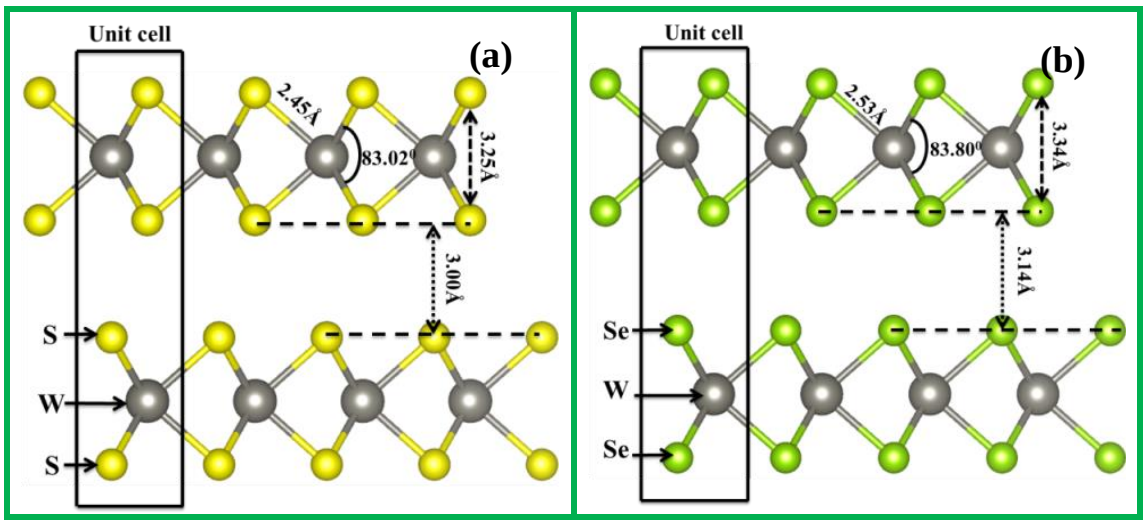


**Figure 6.1** (a) Schematic diagram and corresponding structural parameters of (a) bulk $WS_2$ and (b) bulk $WSe_2$.

### 6.3.1 Electronic properties

The electronic properties of bulk $WS_2$/$WSe_2$and ultrathin WSSe/WSeTe are investigated for solar cell applications. Band structure defines the bandgap of materials and onset of absorption of solar light from VB to CB, which gives the band alignment between the absorber and buffer layer (Pandey et al., 2018). The band alignment defines the open-circuit voltage ($V_{OC}$). The GGA-PBE approach doesn't predict the properties of semiconductor materials accurately. The electronic properties of absorber and buffer material are predicted using mBJ. Band structure and DOS of the absorber materials are computed. The band structure of 2H phase $WS_2$ and $WSe_2$ are shown in Figure 6.2 (a) and Figure 6.2 (c), respectively, using the mBJ. The band structure of absorber materials confirms the CBM at mid of Γ-K point while the VBM is at Γ point of BZ. This confirms the indirect bandgap semiconductor behavior. The bandgap values are around 1.35eV and 1.19eV for 2H $WS_2$ and $WSe_2$ material, respectively. These are in agreement with the reported values (Gusakova et al., 2017). The obtained bandgap of $WS_2$ and $WSe_2$ are suitable for absorber materials in photovoltaic applications(Roy & Bermel, 2018; Wen et al., 2017). The band structure of ultra-thin WSSe and WSeTe structures are also computed and shown in Figure 6.3(a) and Figure 6.3(d), respectively. It illustrates that the CBM and VBM both are located at K point, and thus, confirming the direct band semiconducting behavior. The direct bandgap values are 1.80eV and 1.50eV for ultra-thin Janus WSSe and WSeTe layers, respectively. The obtained band gaps are in agreement or less than with the earlier reports (Hu et al., 2018). The PDOS calculated to understand the contribution of atomic orbitals in the band structure.

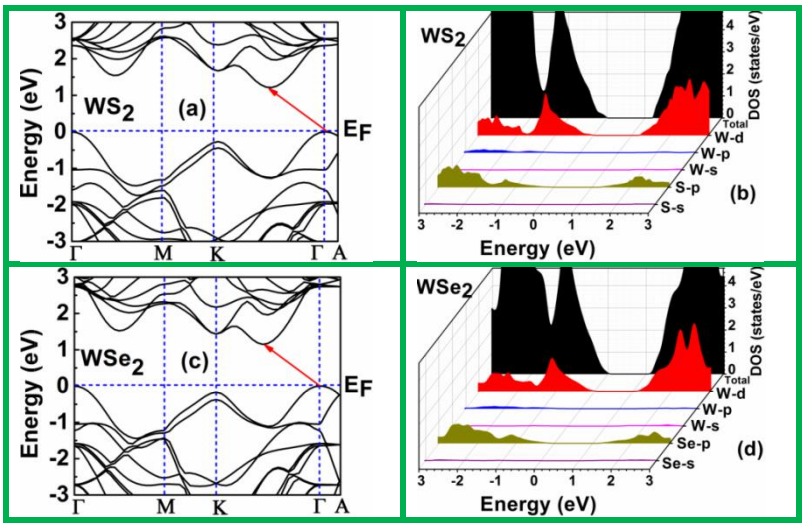


**Figure 6.2** (a) Band structure of $WS_2$ (b) TDOS & PDOS of bulk $WS_2$ (c) Band structure of $WSe_2$ and (b) TDOS & PDOS of bulk $WSe_2$

Figure 6.2(b) validates the bandgap of $WS_2$ absorber materials through the TDOS. Electronic states in VBM are mainly contributed by the W-d and S-p orbitals, and these also show the long-range of hybridization. The hybridization of energy states of W-d and S-p orbital in the VB is confirms the covalent bonding, which promotes the transfer of electrons from VB to CB due to absorption of Sunlight (Pandey et al., 2018). Similar observation is also noticed in the DOS of bulk $WSe_2$, which shows the forbidden region equal to observed electronic bandgap. The VBM and CBM both consist of W-d and Se-p orbitals, which are hybridized like the bulk $WS_2$. Long-range hybridization in the VB and CB is essential to improve the optical absorption, which also leads to the improved photovoltaic performance of the solar cell. The high absorption coefficient of the absorber materials leads to large number of electron and hole pair generation and thus, improving the efficiency of a solar cell device. The s orbital contribution of W and S/Se atom don't lie near to the Fermi level because it is filled and acts as a core electron. The TDOS and PDOS of the buffer layer WSSe and WSeTe materials are shown in Figure 6.3(b) and Figure 6.3(d),

respectively. The DOS of WSSe and WSeTe are similar to that of the bulk $WS_2$ and $WSe_2$, means the VBM and VBM both consist of W-d, S/Se-p, and Se/Te-p orbitals. These also hybridize in the long-range due to the presence of in-plane covalent bonding between transition metal and chalcogen elements. The detailed structural and electronic properties of absorber materials and buffer materials are discussed. Now, we focus on the derivative properties, which are valuable to obtain the performance of a solar cell device using SCAPS-1D simulator.

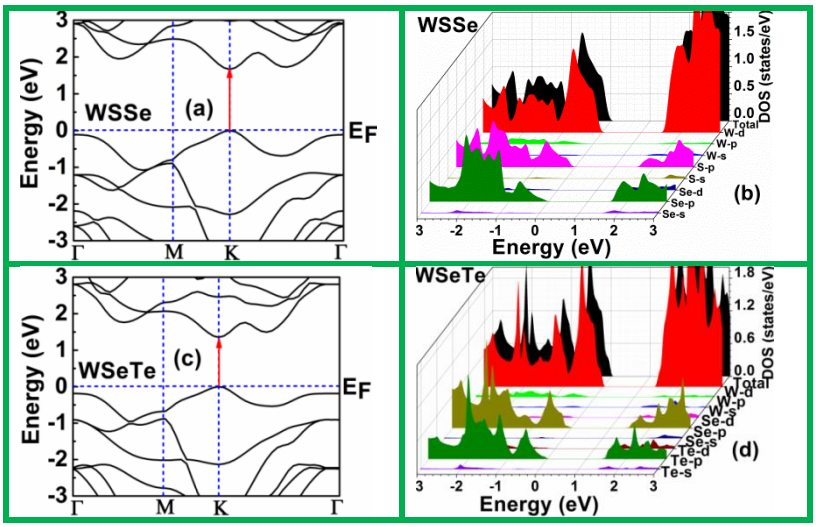


**Figure 6.3** (a) Band structure of WSSe (b) TDOS & PDOS of WSSe monolayer, (c) band structure of WSeTe and (b) TDOS & PDOS of WSeTe monolayer.

The derivative properties are such as the effective mass of electron and hole, computed by fitting the parabola for a small range of wave vector along with the CBM and VBM, respectively. Effective mass is obtained using the expression given below.

$$m^* = \hbar^2 / \left( \frac{d^2E}{dK^2} \right)$$

Where $\hbar, E$ and $K$ are the reduced Planck constant, energy, and wave vector, respectively. The obtained electron and hole effective masses are listed in table 2. The DOS in the VB and CB are calculated using the effective mass through the equation given below (Green, 1990).

The DOS in the conduction band $N_c = 2 \left[ \frac{2\pi m_e K_B T}{h^2} \right]^{\frac{3}{2}}$,

The DOS in the valence band $N_v = 2 \left[ \frac{2\pi m_h K_B T}{h^2} \right]^{\frac{3}{2}}$

In the above expression,$m_e$ and $m_h$ are electron and hole effective masses, respectively. $K_B$is the Boltzmann constant, $T$ is the temperature, and $h$ is the Planck constant. Thermal velocity of electron and hole is calculated using the expression (Cozza, Ruiz, Duch, Simon, & Escoubas, 2016) given below.

$$V_{th} = \sqrt{\frac{3K_B T}{m^*}}$$

In the above expression, $m^*$is the effective mass of electron or hole. Mobility of electron and hole are calculated using formula (Bruzzone & Fiori, 2011; Toriumi, Iwase, & Tango, 1994) given below.

$$\mu = \frac{e\tau}{m^*} = \frac{e\hbar^2 C}{K_B T m^* m_d E_l^2}$$

Where e, τ and $m^*$ are the electronic charge, relaxation time, and effective mass, respectively. $C$ is the elastic constant that is calculated using the relation $2\left(\frac{E-E_0}{E_0 S_0 (\Delta l/l_o)^2}\right)$, $E$ and $E_0$ are the total energy of strained and pristine crystal structure, respectively and $S_0$ is the area of the unit cell. Here $m_d$

is average effective mass determined by $\sqrt{m_x^* m_y^*}$ and $E_l$ is the deformation potential which defines the shift in the edge of CBM or VBM for electron and hole, respectively that can be expressed as $E_l = \Delta E/(\Delta l/l_o)$, where ΔE change in the total energy under the tensile or compression strain, $\Delta l$ is the change in the lattice constant against the tensile and compression strain and $l_o$ is the optimized lattice constant of pristine material. The computed derivative properties are listed in table 2.

### 6.3.2 Optical properties

The optical properties of the materials govern how they will behave under the illumination of light in the solar cell device. The optical properties of materials are computed using real and imaginary part of dielectric constant.

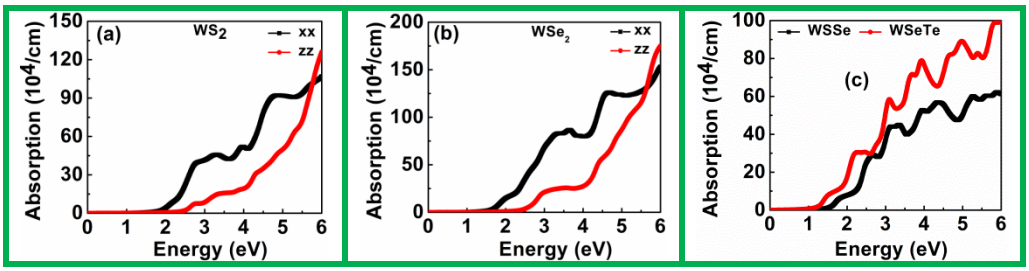


**Figure 6.4** (a) Absorption spectra of bulk $WS_2$, (b) absorption spectra of bulk $WSe_2$ and (c) absorption spectra of WSSe and WSeTe monolayer.

Optical absorption coefficient of absorber and buffer layer is computed using the extinction coefficient expression given below

$$\alpha_{ii} = \frac{2\omega k}{c}$$

Where, $\omega$, $k$, and $c$ are the frequency, extinction coefficient, and light velocity, respectively. Absorption coefficient is the most important property of a material to understand the photovoltaic behavior of the solar cell device. The absorption coefficients of absorber and buffer materials are very small below the bandgap. Here, we have considered the absorption spectra above the bandgap of the material to simulate the solar cell device. The absorption coefficients of the absorber materials $WS_2/WSe_2$ are in the order of $10^5$ $cm^{-1}$, shown in Figure 6.4. Bulk $WS_2$ has a lower absorption coefficient in the visible region as compare to bulk $WSe_2$. So, Bulk $WSe_2$ can absorb more photons and generates more electron-hole pair that improves the efficiency of a solar cell. The absorption coefficient of buffer layers is also in the order of the $10^5$ $cm^{-1,}$ but it is smaller than the absorber layer, shown in Figure 6.4(c). The reflectivity of ultra-thin buffer layers is less, which means most of the photons will be pass to the absorber layer that will help to improve the efficiency of the solar cell devices.

### 6.3.3 SCAPS-1D simulation

The schematic representation of single-junction solar cell is shown in Figure 6.5(a). Here, we considered bulk $WS_2$ and $WSe_2$ as absorber material; ultra-thin WSSe and WSeTe are employed as buffer layers, forming p-n heterojunction. The Al:ZnO is considered as a TCO on the top of the ultra-thin buffer layer, which serves as the transparent front contact in the devices. The photovoltaic device efficiency of bulk TMDs based absorber and ultra-thin Janus structure heterostructure junction is simulated using hybrid approach where the material properties are computed using DFT, and further device performance is simulated using SCAPS-1D (Niemegeers, Burgelman, & Decock, 2016). SCAPS-1D is the one-dimensional numerical solar simulation software which is developed at the Department of Electronics and Information Systems (ELIS) of the University of Gent, Belgium. This one-dimensional SCAPS is capable of simulating the homojunction, multijunction, Schottky barrier, and heterojunction devices. It

employs Poisson's equation, semiconductor carrier transport equations, and continuity equations for electron and hole with suitable boundary conditions to simulate the photovoltaic performance. It is assumed that the entire incident Sunlight enters into the solar cell, i.e. no surface reflection is considered at this end. The computed results under these conditions are comparable to the experimental results under the light and dark conditions. The performance of the solar cell is investigated under the illumination of the light of AM 1.5G solar spectrum. The absorber materials i.e., bulk $WS_2$ and $WSe_2$ are p-type indirect bandgap semiconductors (Cao et al., 2017; Devadasan, Sanjeeviraja, & Jayachandran, 2001; Fang et al., 2012; Kamieniecki et al., 1983; Sommerhalter, Matthes, Boneberg, Lux-Steiner, & Leiderer, 1999; H. Zhou et al., 2015). However, some reports are showing $WS_2$ as an n-type semiconductor due to sulfur vacancy (Carozo et al., 2017). The experimental and theoretical approach investigated the donor and acceptor defects present in the TMDs materials (W. Zhou et al., 2013b). The shallow donor and acceptor defect don't affect the efficiency of solar cell significantly. The defect states are considered in deep around 0.6 eV above the VB in absorber materials. The minority carrier lifetime of bulk $WS_2$ and $WSe_2$ are 25ns and 20ns, respectively. Interface recombination is considered at the interface of the absorber and buffer layer. In addition, interface recombination velocity considered is $10^4$ cm/sec at the p-n interface for the initial structure. Neutral defects are considered in the bulk and p-n interface, so as it doesn't impact the charge neutrality at space charge region. The defect capture cross-section area is $4x10^{-11}$ $cm^2$ considered. The thermal velocity of the electron and hole correspond to absorber and buffer materials are computed and reported in table. 6.2. The back-contact work function is approximated by flat band approximation with surface recombination speed $1.0x10^5$ and $1.0x10^7$ cm/s for electrons and holes, respectively. The radiation recombination coefficient for the absorber and buffer materials is $1.04x10^{-10}$ $cm^3/s$. The computed electronic properties are listed in table.6.2. The optical absorption coefficient of the absorber and ultra-thin Janus layer are shown in Figure 6.4, obtained from the DFT calculation.

**Table 6.2** Material parameter of absorber, buffer, and TCO used to simulate the performance of a solar cells [C denotes the properties calculated using the post processing of DFT data]

| Material properties | WS2 | WSe2 | WSSe | WSeTe | Al:ZnO |
|---|---|---|---|---|---|
| Thickness [μm] | 2 | 2 | 0.01 | 0.01 | 0.2 |
| Bandgap [eV] | 1.35 [C] | 1.19 [C] | 1.80 [C] | 1.50 [C] | 3.37 (Gupta & Dixit, 2018) |
| Electron Affinity [eV] | 4.5 | 4.5 | 4.3 | 4.6 | 4.6 |
| Dielectric permittivity | 8.27 [C] | 13.8 [C] | 4.65 [C] | 8.04 [C] | 9 (Courel, Andrade-Arvizu, & Vigil-Galán, 2015) |
| Density of states in CB [$cm^{-3}$] | $1 \times 10^{19}$ [C] | $8.3x10^{18}$ [C] | $5x10^{18}$ [C] | | $2.2 \times 10^{17}$ (Gupta & Dixit, 2018) |
| Density of states in VB [$cm^{-3}$] | $1.4x10^{19}$ [C] | $1.6x10^{18}$ [C] | $8.3x10^{18}$ [C] | $1.1 \times 10^{18}$ [C] | $1.8 \times 10^{18}$ (Gupta & Dixit, 2018) |
| Thermal velocity of electron [cm/s] | $1.6x\ 10^7$ [C] | $1.7 \times 10^7$ [C] | $2 \times 10^7$ [C] | $1.9\ x10^7$ [C] | $2.1 \times 10^7$ (Gupta & Dixit, 2018) |
| Thermal velocity of hole [cm/s] | $1.4 \times 10^7$ [C] | $1.4 \times 10^7$ [C] | $1.7x\ 10^7$ [C] | $1.55 \times 10^7$[C] | $1.4 \times 10^7$ (Gupta & Dixit, 2018) |
| Electron mobility [$cm^2/Vs$] | 60 (Schmidt, Giustiniano, & Eda, 2015a) | 100 (Schmidt et al., 2015a) | 112 [C] | 263 [C] | 150 (Gupta & Dixit, 2018) |

| | | | | | |
|---|---|---|---|---|---|
| Hole mobility [$cm^2/Vs$] | 95 (Schmidt et al., 2015a) | 500 (Schmidt et al., 2015a) | 233 [C] | 470 [C] | 25(Courel et al., 2015) |
| Donor concentration [$cm^{-3}$] | 0 | 0 | 1 x $10^{19}$ | 1 x $10^{19}$ | 1x$10^{20}$ (Gupta & Dixit, 2018) |
| Acceptor concentration [$cm^{-3}$] | 1 x $10^{16}$ | 1 x $10^{16}$ | 0 | 0 | |
| Absorption coefficient [$cm^{-1}eV^{1/2}$] | File | File | File | File | |
| Radiative recombination coefficient [$cm^{-3}/s$] | 1.04 x $10^{-10}$ | 1.04 x $10^{-10}$ | 1.04 x $10^{-10}$ | 1.04 x $10^{-10}$ | |
| Effective mass electron | 0.54 [C] | 0.48 [C] | 0.34 [C] | 0.38 [C] | 0.275(Courel et al., 2015) |
| Effective mass hole | 0.67 [C] | 0.74 [C] | 0.48 [C] | 0.57 [C] | 0.59(Courel et al., 2015) |
| Hole capture cross section ($cm^2$) | 4x $10^{-11}$ | 4x $10^{-11}$ | 1x $10^{-15}$ | 1x $10^{-15}$ | 1x $10^{-15}$ (Gupta & Dixit, 2018) |
| Electron capture cross section ($cm^2$) | 4x $10^{-11}$ | 4x $10^{-11}$ | 1x $10^{-15}$ | 1x $10^{-15}$ | 1x $10^{-15}$ (Gupta & Dixit, 2018) |
| Defect density[$cm^{-3}$] | 1x $10^{11}$ | 1x $10^{11}$ | | | |
| Minority carrier lifetime | 25ns | 20ns | | | |
| Interface recombination speed (cm/s) | $10^4$ | $10^4$ | | | |
| Defect type at bulk/interface | Donor/Neutral | Donor/Neutral | | | |

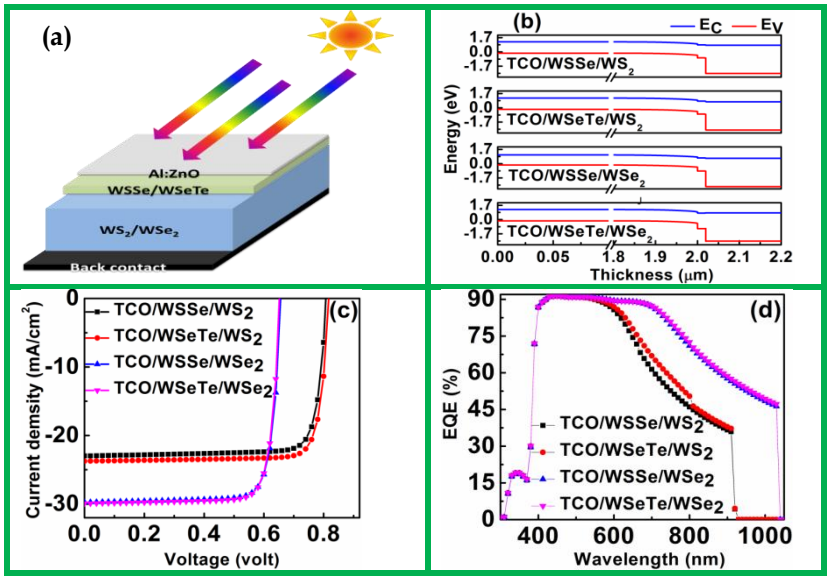


**Figure 6.5** (a) Schematic representation of solar cell device, (b) band alignment at interface (c) J-V curve and (d) EQE of TCO/WSSe/$WS_2$, TCO/WSeTe/$WS_2$, TCO/WSSe/$WSe_2$ and TCO/WSeTe /$WSe_2$ solar cell devices.

### 6.3.4 Single junction solar device analysis

Single junction solar cell performances with bulk W(S/Se)$_2$ absorber layers and ultra-thin WSSe and WSeTe buffer layers are investigated by considering the materials parameters listed in table 6.2. Current-voltage characteristics for the four possible, i.e., TCO/WSSe/$WS_2$, TCO/WSeTe/$WS_2$, TCO/WSSe/$WSe_2$, and TCO/WSeTe/$WSe_2$ heterostructure solar cells is shown in Figure 6.5(c) and the corresponding external quantum efficiency (EQE) spectra is shown in Figure 6.5(d). The obtained PV performance of the device dictates that the photo response

mainly depends on the bandgap of the absorber layer and band alignment between the absorber and buffer layer, shown in Figure 6.5(b). Solar cell characteristics, Figure 6.5(c) illustrate that $WS_2$ absorber based solar cell has high $V_{OC}$ and small $J_{SC}$ as compared to the $WSe_2$ absorber based solar cell. The PV response is following the fact that high bandgap materials work like a transparent for small energy photon and not contribute to the photocurrent generation. This result is validated from the EQE plot of these heterostructures, as shown in Figure 6.5(d). Bulk $WS_2$ absorber covers the small area in EQE over the bulk $WSe_2$ based solar cell, which ensures the small current density of $WS_2$ over the $WSe_2$ based solar cell. The $WS_2$ based solar cell showed a high $V_{OC}$ over $WSe_2$ due to high bandgap. Maximum $J_{SC}$ and the $V_{OC}$ observed are (22.97mA/cm², 0.82V), (23.74mA/cm², 0.82V), (29.73 mA/cm², 0.66V) and (29.92 mA/cm², 0.66V) for TCO/WSSe /$WS_2$, TCO/WSeTe /$WS_2$, TCO/WSSe/$WSe_2$ and TCO/WSeTe/$WSe_2$ solar cell, respectively.

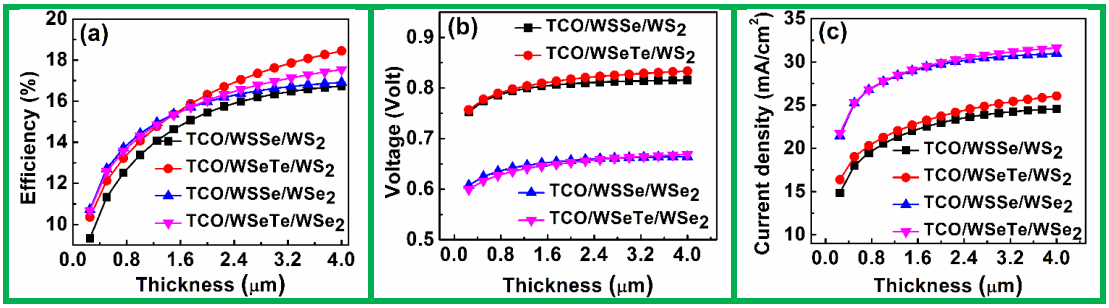


**Figure6.6** Effect of acceptor layer thickness on (a) efficiency (b) open circuit voltage and (c) short circuit current of TCO/WSSe/$WS_2$, TCO/WSeTe/$WS_2$, TCO/WSSe/$WSe_2$ and TCO/WSeTe /$WSe_2$ solar cell devices.

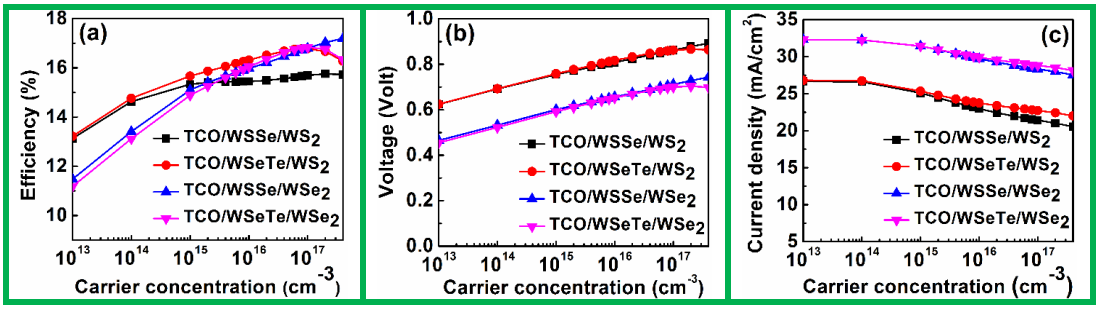


**Figure 6.7** Effect of acceptor layer carrier concentration on (a) efficiency (b) open circuit voltage and (c) short circuit current of TCO/WSSe/$WS_2$, TCO/WSeTe/$WS_2$, TCO/WSSe/$WSe_2$ and TCO/WSeTe /$WSe_2$ solar cell devices.

### 6.3.5 Effect of absorber layer thickness

The thickness of the absorber layer should be optimum to absorb all the photons coming from the buffer layer. The effect of absorber layer thickness on photovoltaic performance is examined through η, Voc, and Jsc, and shown in Figure 6.6. The η of the solar cell devices increases exponentially with increasing the thickness of the absorber layer up to 3μm and further increasing the thickness, the improvement in the current density is small. All considered solar cells follow a similar trend in improving efficiency for thickness variation. The Voc is almost constant for all the solar cells by varying the thickness of the absorber materials. The Jsc is increasing with enhancing the absorber layer thickness, and the resultant efficiency of the solar cell devices is increasing with absorber thickness. About 3μm thickness is sufficiently large to achieve the maximum photovoltaic response for the considered solar cells. The enhancement in efficiency with increasing the thickness of the absorber layer can be explained in terms of Beer Lamberts law $I = I_0 e^{-\alpha x}$, which suggests the enhanced photon absorption in the absorber layer induces more electron-hole pairs, and thus, increasing Jsc. Moreover, the Voc is changing slightly due to the generation of electron-hole pairs in the solar cell.

### 6.3.6 Effect of the absorber layer carrier concentration

The carrier concentration of absorber materials is varied in the range of the $1x10^{14}$ to $1x10^{18}$ $cm^{-3}$. It is observed from Figure 6.7 (a) that the η increases linearly for small carrier concentrations, and after a saturation, it decreases with increasing carrier concentration. The maximum efficiency for the heterostructure junctions under considerations are obtained for ~ $1x10^{17}$ $cm^{-3}$ carrier density. The improvement in Voc is due to the enhanced carrier concentration according to the relation

$$V_{oc} = \frac{kT}{q} ln\left(\frac{I_L}{I_0} + 1\right)$$

However, the Jsc of the device reduces as enhanced carrier concentration reduces the effective depletion width penetrated inside the absorber layer, which condenses the separation of photogenerated charge carrier and collected at the external contact. Figure 6.7(c) shows that Jsc starts decreasing as the absorber layer carrier concentration goes beyond $1x10^{14}$ $cm^{-3}$ while Voc increases. This is because of the reduction in the depletion width at higher concentration at the absorber site. Also, the lifetime of photogenerated charge carrier reduces the charge collection probability, and as a result, the Jsc reduces. Maximum η observed 15.8, 16.7, 17.82 and 18.8 for TCO/WSSe/$WS_2$, TCO/WSeTe/$WS_2$, TCO/WSSe/$WSe_2$ and TCO/WSeTe /$WSe_2$ solar cell device, respectively.

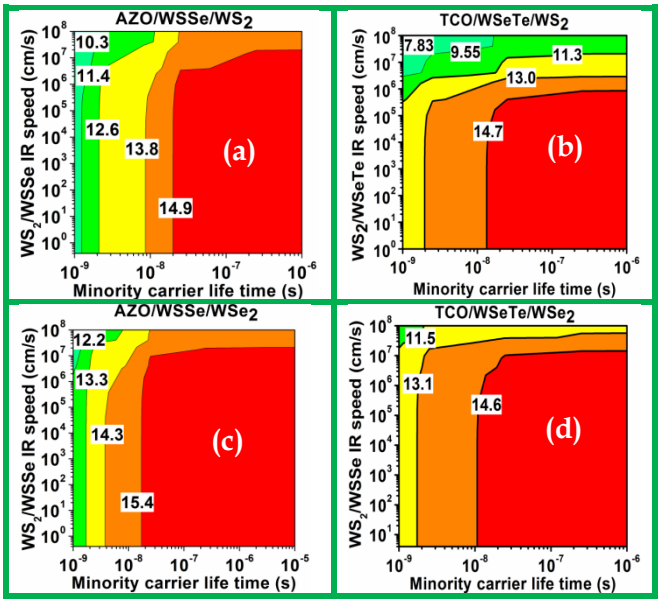


**Figure: 6.8** Contour plot of interface recombination speed at interface versus minority carrier life time of (a) AZO/WSSe/$WS_2$ (b) AZO/WSeTe/WS2 (c) AZO/WSSe/$WSe_2$ and (d) AZO/WSeTe/$WSe_2$ solar cell devices

### 6.3.7 Impact of defect density in the absorber layer and interface recombination speed at heterojunction

There is lack of literature for $WS_2$ and $WSe_2$ materials, but $MoS_2$ belongs to the same family of systems, so here, we considered and related the properties of $MoS_2$ to understand $W(S/Se)_2$ materials. Tongay et al. (Tongay et al., 2013) studied the pristine $MoS_2$ monolayer doesn't respond to the $N_2$ molecule. However, it reacts only to the sulfur vacancy site in $MoS_2$ and binds to it. The formation energy of $N_2$ molecule very from 90meV to 150meV depending upon the type of vacancy in TMDs. The $N_2$ molecule adsorbed on $MoS_2$ monolayer creates the defect states around 0.2 eV above the VB and the other is 0.3 eV below the CB. Oxygen molecule adsorbs on the cracks/defect site of $MoS_2$ surface and at high annealing temperature performs the p-type semiconductor behaviour. The similar results are also investigated using the DFT calculations (Nan et al., 2014). Yuan et al. (S. Yuan, Roldán, Katsnelson, & Guinea, 2014) investigated that the

tungsten and sulfur vacancy defect introduce the trap states at 0.18eV and -0.86eV, respectively. The η of the solar cell is not changing correspond to the lower defect density due to defect generated charge carrier scattering (Gupta & Dixit, 2018). Further, enhancing the defect density above $10^{10}$ $cm^{-3}$, the η linearly decreases and approaches to negligible around ~ $1x10^{15}$ $cm^{-3}$. The interface defect density should be the lowest to obtain enhanced performance of a solar cell. The absorber defect density of $WS_2/WSe_2$ defines the minority carrier lifetime using the equation $\tau = \frac{1}{\sigma * V_{th} * N_t}$. In addition, p-n junction interface defect density affects the interface recombination speed (cm/s), can be defined as $V_{IR} = \sigma * V_{th} * N_{IR}$. Here, σ, $V_{th}$, $N_t$ and $N_{IR}$ are the capture cross section area, thermal velocity, absorber defect density, and interface defect density, respectively. The impact of interface recombination speed and minority charge carrier on the η of AZO/WSSe/$WS_2$, AZO/WSeTe/$WS_2$, AZO/WSSe/$WSe_2$ and AZO/WSeTe/$WSe_2$ solar cell device are illustrated in contour plot in Figure 6.8. The contour plot suggests that high minority carrier life time (s) and small interface recombination speed leads to improve the photovoltaic performance of the solar cell.

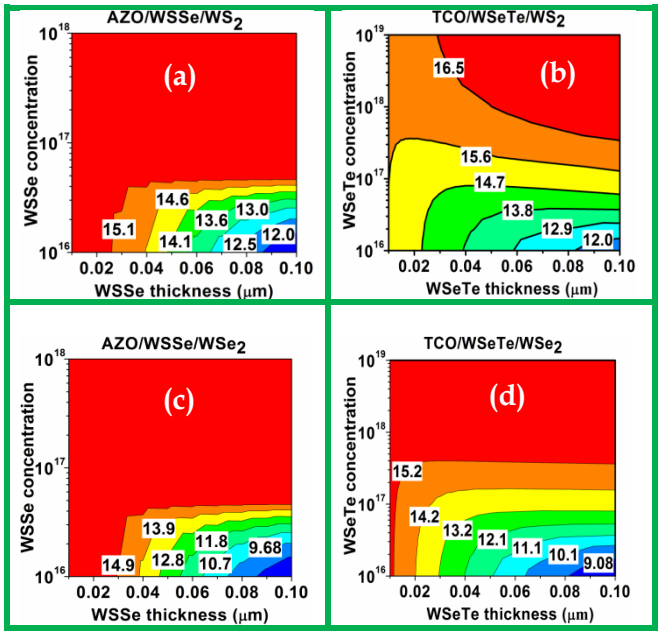


**Figure: 6.9** Contour plot of an acceptor layer carrier concentration versus thickness of buffer layer of (a) AZO/WSSe/$WS_2$ (b) AZO/WSeTe/$WS_2$ (c) AZO/WSSe/$WSe_2$ and (d) AZO/WSeTe/$WSe_2$ solar cell devices

### 6.3.8 Effect of buffer layer thickness and carrier concentration

$WS_2$ bulk and monolayer has been considered as a buffer layer and found that monolayer exhibits the improved η around 20.48% over the bulk with η around 15.19% (Roy & Bermel, 2018). By considering this fact, we considered newly explored WSSe and WSeTe monolayers as a buffer layer. The buffer layer impact on the PV performance is examined in terms of the donor concentration, electron affinity, and thickness. The high bandgap and ultrathin layer of buffer provide more photon for absorption on the surface of the absorption layer with small absorption loss at the buffer layer. The donor carrier concentration effect on the PV performance is investigated and found that η enhances with carrier concentration. Further, increasing the carrier concentration above $1x10^{19}$ $cm^{-3}$, the η saturates. So, to find the optimal device performance, the donor carrier concentration should be optimum. A similar observation has been demonstrated for $WS_2$ based monolayer as a buffer layer by Roy et al. (Roy & Bermel, 2018). The donor carrier concentration and thickness effect on the η is illustrated in the contour plot, shown in Figure 6.9. The thickness of the donor layer is varied from 0.01μm to 0.10μm, and carrier concentration from $1x10^{16}$ $cm^3$ to $1x10^{18}$ $cm^{-3}$. At low carrier concentration, with increasing the thickness, the efficiency is decreasing, Figure 6.9. The efficiency of the solar cell devices is increasing by keeping small

thickness and increasing the carrier concentrations. The high carrier concentration of donor layer enhances the depletion width inside the absorber layer, and reduced thickness decreases the absorption loss

$$W_d = \left[\frac{2\varepsilon_1\varepsilon_2(V_{bi}-V)(N_A^2+N_D^2)}{q(\varepsilon_1 N_D+\varepsilon_2 N_A)N_D N_A}\right]^{1/2}$$

Where q, $\varepsilon_1$, $\varepsilon_2$, $N_D$, $N_A$, $V_{bi}$, and V are the electron charge, dielectric permittivity absorber, buffer material, donor concentration, acceptor concentration, built-in potential and applied voltage, respectively.

After optimizing all the solar cell parameters, Figure 6.10 shows the (a) J-V and (b) QE plot on the optimized parameters of considered solar cells. The efficiency of a solar cell depends on the Jsc, Voc, and fill factor. The thickness of the buffer layer should be minimum to pass the light photon to the absorber layer. The Jsc improves with the thickness of the absorber layer. Moreover, the Voc is enhanced with the carrier concentration. The defect density and interface defect density should be minimum as possible to get maximum efficiency. The maximum efficiency obtained are 17.73%, 18.87%, 18.87% and 18.1% for ZO/WSSe/$WS_2$, AZO/WSeTe/$WS_2$, AZO/WSSe/$WSe_2$ and AZO/WSeTe/$WSe_2$ solar cell device, respectively. The obtained efficiency of the considered solar cells is within the limit of the Schockley-Queisser limit (Shockley & Queisser, 1961).

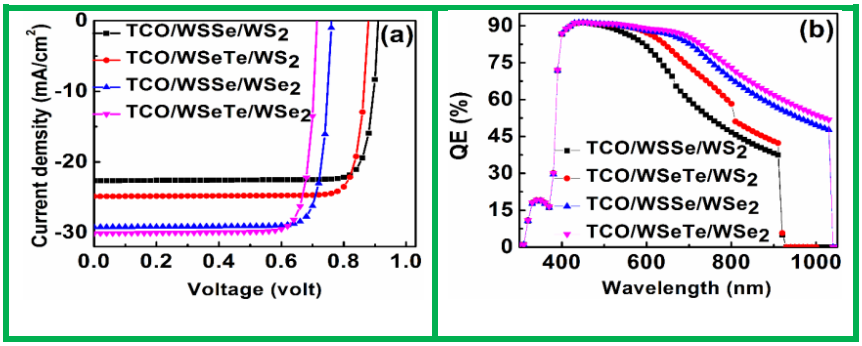


**Figure6.10** (a) J-V and (b) QE plot based on the optimized parameters of considered solar cells

## 6.4 Conclusion

In this chapter, optoelectronic properties of bulk $WS_2$/$WSe_2$ materials make them suitable absorber materials for solar cell application. The ultra-thin WSSe/WSeTe layer have low absorption coefficient which ensure that they used as buffer layer. The electronic and other properties are calculated from DFT required to simulate the performance of solar cell using SCAPS-1D simulator. The PV performance is investigated through the η, Jsc, Voc and fill factor. The effect thickness, carrier concentration and carrier concentration of absorber and buffer layer on PV performance investigated. The impact of minority charge carrier and interface recombination speed are considered towards the solar cell more realistic. After considering these effects, we optimized the maximum possible efficiency of solar cell.